Research Square

Preprints are preliminary reports that have not undergone peer review.
They should not be considered conclusive, used to inform clinical practice,
or referenced by the media as validated information.

Minimal metabolite assembly kinetics revealing a novel role for chaperones

Daniel Otzen

dao@mbg.au.dk

Aarhus University

Jeremias Widmann

Aarhus University

Carl Linnemann

Aarhus University https://orcid.org/0000-0003-3427-597X

Carsten Scavenius

Aarhus University

Janni Nielsen

Aarhus University

Samuel Peña-Díaz

Aarhus University

Sourav Kumar

Tel Aviv University

Dana Laor Bar Yosef

Tel Aviv University https://orcid.org/0000-0003-1699-3839

Daniel Segal

Tel Aviv University

Ehud Gazit

Tel Aviv University https://orcid.org/0000-0001-5764-1720

Martin Bremholm

Aarhus University https://orcid.org/0000-0003-3634-7412

Article

Keywords: Amyloid, Inborn errors of metabolism, Chaperones, Kinetics, Small molecules

Posted Date: November 24th, 2026

DOI: https://doi.org/10.21203/rs.3.rs-11555353/v1

License: This work is licensed under a Creative Commons Attribution 4.0 International License.
Read Full License

Additional Declarations: There is **NO** Competing Interest.

Minimal metabolite assembly kinetics revealing a novel role for chaperones

Jeremias Widmann[1], Carl J. Linnemann[2], Carsten Scavenius[1], Janni Nielsen[1], Samuel Peña-Díaz[1], Sourav Kumar[3], Dana Laor Bar-Yosef[3], Daniel Segal[3], Ehud Gazit[4], Martin Bremholm[2], Daniel E. Otzen[1]*

[1] Department of Molecular Biology and Genetics, Aarhus University, Universitetsbyen 2, 8000 Aarhus C, Denmark

[2] Department of Chemistry, Aarhus University, Langelandsgade 140, 8000 Aarhus C, Denmark

[3] The Shmunis School of Biomedicine and Cancer Research, George S. Wise Faculty of Life Sciences, Tel Aviv University, Tel Aviv, 6997801, Israel

[4] The Department of Materials Science and Engineering, The Iby and Aladar Fleischman Faculty of Engineering, Tel Aviv University, Tel Aviv 6997801, Israel

* To whom correspondence should be addressed at dao@mbg.au.dk

Key words (5):

Amyloid, Inborn errors of metabolism, Chaperones, Kinetics, Small molecules

ABSTRACT:

Inborn errors of metabolism lead to the toxic accumulation of metabolites, a process that is associated with the onset of severe disorders like Phenylketonuria or Gaucher disease. Numerous studies have shown that these metabolites can form amyloid-like assemblies upon accumulation. Yet the mechanisms underlying their self-assembly and cellular regulation remain unclear. Here we show that three disease-associated metabolites, adenine, glucosylceramide and phenylalanine, self-assemble through different non-canonical pathways, including polymorphic restructuring, clustering and concentration-dependent pathway switching. Minimal phenomenological kinetic models quantitatively captured these behaviours across broad concentration ranges, providing a unified framework for metabolite self-assembly. Through interactome analyses of cellular lysates we identified multiple molecular chaperones associated with metabolite assemblies. Kinetics analysis of selected chaperones revealed that they target specific assembly steps such as nucleation, elongation, and remodelling the assembly pathways. These findings demonstrate molecular chaperones as modulators of metabolite aggregation and extend their role beyond classic proteostasis towards metabolostasis.

Abbreviations:

Ade: Adenine; CD: Circular Dichroism; CSD: Cambridge Structural Database; DHA: 2,8-dihydroxyadenine; FTIR: Fourier Transform Infrared Spectroscopy; GD: Gaucher disease; GlcCer: Glucosylceramide; Hsc70iP: Heat shock cognate 71 kDa protein interacting protein; Hspβ1: Heat shock protein β-1; IEM: Inborn Error of Metabolism; IPTG: Isopropyl-β-D-thiogalactopyranosid; NPAC: Nascent polypeptide-associated complex subunit α; Phe: Phenylalanine; ODE: ordinary differential equation; PKU: Phenylketonuria; PXRD: Powder X-ray Diffraction; TEM: Transmission Electron Microscopy; ThT: Thioflavin T.

Introduction:

Mutations in key metabolic enzymes lead to metabolic disorders collectively termed inborn errors of metabolism (IEM) underlie a group of severe disorders characterized by pathological metabolite accumulation.[1] Symptoms resulting from IEM are quite diverse, ranging from neurological deficiencies in Phenylketonuria (PKU) to infant mortality in Gaucher disease (GD) type II.[2,3] Although individually rare, collectively IEMs affect around 1 in 2,500 newborns and account for approximately 15 % of all single gene disorders.[2,3]

However, the underlying molecular mechanisms correlating the observed mutations with the progression of the disease remain incompletely understood. Nevertheless, recent studies have shed some light, uncovering a striking similarity between IEMs and proteinopathies, as both involve the accumulation of pathological amyloid-like self-assemblies.[4] Mirroring the diversity of protein amyloids, metabolite self-assemblies can originate from various molecular classes such as the sphingolipid glucosylceramide (GlcCer) associated with GD, amino acids like phenylalanine (Phe) in PKU and nucleobases such as adenine (Ade) in 2,8-dihydroxyadenine (DHA) crystalline nephropathy (**Fig. S1**).[4-6] Metabolite self-assemblies were shown to form in yeast derived disease model systems and are found in patient-derived tissue.[4,6] Moreover, these abnormal metabolite structures share several hallmarks with protein amyloids, including fibrillar morphology, affinity towards amyloid-specific dyes, and interactions with amyloidogenic proteins.[7] However, as metabolite assemblies are non-proteinaceous, canonical models of amyloid growth, based on structural rearrangements of the polypeptide backbone, cannot adequately describe their assembly mechanisms.

Determining how these aggregates are formed also raises the key question of whether this self-assembly process and its products could be regulated by natural chaperones, which in turn play central roles in controlling protein aggregation.[8,9] To date, only polyphenols like epigallocatechin gallate, as well as classic chemical chaperones like trimethylamine N-oxide (TMAO) and dimethyl sulfoxide (DMSO), have been found to inhibit metabolite self-assembly.[10,11] Nevertheless, cellular studies have reported the upregulation of heat-shock proteins in response to metabolite accumulation, raising the possibility that chaperones directly participate in regulating metabolite self-assembly.[6,12]

In the present work, we addressed these major questions and studied the ability of molecular chaperones to interact with and regulate metabolite self-assemblies, using Ade, GlcCer, and Phe as representatives of chemically distinct metabolites. First, we employed orthogonal structural and kinetic approaches to characterize the assembly mechanisms of selected metabolites across a broad concentration range and to determine whether a common mechanistic framework could account for their divergent behaviours. In parallel, chaperone candidates were identified in a mass spectrometry-based interactome analysis. Subsequently, selected molecular chaperones were examined to establish whether they act as nonspecific inhibitors or instead modulate

specific nucleation, elongation, and state-transition steps. This approach enabled the assessment of whether the same principles that modulate proteostasis also extend to the regulation of metabolite assemblies and, consequently, metabolostasis.[13] As a result, we discovered distinct chaperones that slow down and redirect metabolite self-assembly, extending proteostasis principles to non-proteinaceous molecules.

Methods:

Materials:

Flat bottom clear 96 well polystyrene microplates (Corning Inc) were used for plate reader assays. GlcCer (C16:1 glucosyl(β) ceramide (d18:1/16:0)) was from Avanti Polar Lipids Inc. Plasmids were from GenScript and Twist Bioscience. Ultrapure water was produced by Milli-Q filtration (Merck Millipore). All other chemicals such as Ade, Phe, ThT and buffer salts were from Sigma Aldrich of the highest purity available. Stock solutions of Ade and Phe were prepared on the same day by dissolving into 1× PBS buffer at pH 7.4 to 80 mM and 200 mM, respectively, followed by incubation at 90 °C for 3 h before gradually cooling down. GlcCer was dissolved to 10 mM in 100 % DMSO, aliquoted and stored at -20 °C. Unless stated otherwise, all assays were performed at 37 °C in PBS (pH 7.4).

Thioflavin T (ThT) assay

Two different plate readers, FluoStar Plus Multimode Microplate Reader (BMG Labtech) and Tecan Infinite M1000 plate reader (Tecan), were used to monitor both self-assembly of metabolites as well as interactions with chaperones using time dependent changes in ThT fluorescence. Assays were performed in technical triplicates in 96-well microplates at a total volume of 150 µL per well using an excitation wavelength of 448 nm and emission at 485 nm. Each reaction contained a 2 mm diameter autoclaved glass bead, 40 µM ThT and metabolite stock solution diluted to the desired concentration. ThT alone in buffer served as background. When investigating inhibitory effects of chaperones, chaperones were added at a concentration of 10-100 µM. Fibrillation was monitored continuously with orbital shaking at 300 rpm for a minimum of 24 up to 144 h.

Turbidity assay

Turbidity changes, measured at absorption at 350 nm, were followed in a ClarioStar Plus Multimode Microplate Reader (BMG Labtech) as orthogonal approach for monitoring metabolite self-assembly. Assays were performed as described for the ThT assay, except that ThT was omitted. Metabolite-free solution was used as control.

Capture of self-assembly intermediates

To capture and analyse intermediates of self-assembly, metabolites were diluted to desired concentrations from freshly prepared stock solutions in 96-well microplates in a

total volume of 150 µL per well. One row of wells was monitored over time by ThT fluorescence serving as reference. All other rows were incubated without ThT, aliquoted at certain timepoints and either used directly for analysis as liquid samples or flash frozen in liquid nitrogen. Frozen samples were lyophilized and stored dry at room temperature until further use.

Circular Dichroism

CD was used to monitor initial self-assembly kinetics of Phe. Freshly prepared metabolite stock solution or empty solution accounting for background was diluted to desired concentration to a total volume of 0.3 mL, transferred to a 0.1 mm quartz cuvette and monitored at 223 nm, chosen to maximize signal change, using a Chirascan V-100 CD Spectrometer (Applied Photophysics).

Fourier-Transform Infrared Spectroscopy (FTIR)

FTIR was conducted by applying 3 µL of liquid sample onto a KBr infrared measuring glass and drying with constant nitrogen flow. Scans were recorded from 4000 to 625 cm^{-1} with 64 repeats at 0.5 cm^{-1} resolution in a Bruker Tensor 27 IR spectrometer (Bruker).

Transmission electron microscopy (TEM)

Grids for TEM were prepared by applying 3 µL of liquid sample on Formvar supported carbon-coated 400 mesh copper grid for 2 min. After removing excess liquid, negative staining was done by incubating 3 µL of 2 % uranyl acetate solution on grids for 1 min, followed by removal of excess fluid. Before use, grids were dried for at least another 5 min. The samples were imaged on a G2 Spirit electron microscope (Tecnai), operated at 80 kV.

Powder X-ray diffraction (PXRD)

PXRD was used to analyse structural changes over time in Ade and Phe self-assembly by collecting PXRD diffractograms of dry captured intermediates and endpoints. The powder was placed evenly onto a zero-background silicon plate sample holder. PXRD collection was done in symmetric Bragg-Brentano geometry in a Rigaku SmartLab X-ray diffractometer (Rigaku) with a Cu Kα radiation source for an angular range from 5 deg to 90 deg (2θ). Patterns were consequently used to search for known polymorphs deposited in the Cambridge Structural Database (CSD). Best matching polymorphs, as well as salt formations possibly formed by buffer composition were then fitted to the experimental pattern by Rietveld refinement to extract the actual polymorph distribution. Refinements can be found in the supplementary.

Protein expression

Genes of interest were DnaK, Skp, GroEL and GroES from *E. coli*, as well as DnaJ homolog subfamily C member 8 (DnaJC8), Nascent polypeptide-associated complex subunit α

(NPAC), Heat shock protein β-1 (Hspβ1) and Heat shock cognate 71 kDa protein interacting protein (Hsc70iP) from human origin. These were codon optimized for *E. coli* expression and cloned into pET28a(+) vectors by Genscript. Depending on *in silico* prediction of terminus accessibility, either an N- or C-terminal 6x His-tag and TEV protease cleavage site was included. Complete sequences with tag insertions are provided in the Appendix. Expression plasmids were inserted into *E. coli* strain C43 by electroporation before expression by Isopropyl-β-D-thiogalactopyranosid (IPTG) induction. Proteins were purified with Ni-NTA beads: 1 mL of 50 % packed beads suspended in binding buffer (1× PBS, pH 8, containing cOmplete protease inhibitor as recommended by producer, 2 M Urea and 10 mM imidazole) was incubated with 4 mL of concentrated cell lysate for 1 h at 4 °C. In total 4 mL of beads were used for each production culture. Subsequently beads were loaded onto PD10 filter columns and washed twice with 1 column volume of washing buffer (1× PBS, pH 8, containing cOmplete protease inhibitor as recommended by producer, 2 M Urea and 20 mM imidazole) before eluting with 1 mL of elution buffer (1× PBS, pH 8, containing cOmplete protease inhibitor as recommended by producer, 2 M Urea 250 mM imidazole). After rebuffering into fresh 1× PBS buffer (pH 7.4) and measuring concentration using absorption at 220 nm, aliquots of 100 µL were stored at -20 °C.

Pulldown assay to identify chaperones binding to metabolite self-assemblies

E. coli and SH-SY5Y cells were grown at 37 °C in LB and DMEM medium with 10% FCS and 1% pen-strep, respectively. *E. coli* cultures were lysed by sonication in lysis buffer and SH-SY5Y cells by repeated freeze-thaw cycles. Cell debris was removed by centrifugation at 4000 g before sterile filtration with 0.2 µm filter units. 50 µL of cell lysate were incubated for 20 min in 30000 MWCO NanoSep filter tubes with 450 µL preformed metabolite self-assemblies, directly taken from turbidity assay plate after completion of aggregation at each of the different assembly phases. Metabolite free buffer solution was used as negative control. Bait used to obtain phase specific interactomes included 50 µM of α-synuclein (positive control), 30 mM and 80 mM Ade, 150 µM GlcCer as well as 5 and 200 mM Phe. To retain only proteins interacting with metabolite self-assemblies, the solution was spun down at 14000 g for 20 min followed by two consecutive washing steps with the corresponding metabolite solution to avoid concentration dependent morphology changes in the metabolite assemblies. To elute the interactome, the filter cake was incubated in 100 µL of 6 M Guanidinium chloride and incubated for 1 h before spinning down and buffer exchange to 1× PBS. After analysis of individual fractions by SDS-PAGE, samples were analyzed by MS/MS. Samples were washed twice with 8 M urea, once with 8 M urea containing 50 mM DTT, once with 8 M urea containing 50 mM iodoacetamide, and again twice with 8 M urea on a 10 kDa MWCO filter unit. Washes were centrifuged down at 14000 g for 30 min. After subsequent trypsin digestion at 37 °C with 0.25 µg of sequencing-grade trypsin in 50 mM ammonium bicarbonate, peptides were

acidified with 0.1 % trifluoroacetic acid and micro-purified using POROS R2-packed pipette tips.

SDS-PAGE

Sodium dodecyl sulphate polyacrylamide gel electrophoresis (SDS-PAGE) was carried out according to the protocol of Laemmli.[14] 10 µL of sample and 5 µL of molecular weight marker were loaded onto the gel. Constant voltage of 180 V was applied until the dye front reached the end of the gel, followed by staining and destaining.

Fitting

Nonlinear correlation of aggregation velocity and initial monomer concentration were fitted using preinstalled functions (Michaelis-Menten, Hill, Hill1 and substrate inhibition) in OriginLab 2024 shown in Supplementary Information.

Ordinary differential equation (ODE) systems were fitted to experimental data using Python (SciPy). ODE systems can be found in Supplementary Information.

Results:

Biphasic self-assembly behaviour of Adenine constituted by polymorphic changes

To enable a systematic analysis of chaperone-metabolite interaction we first needed to uncover a minimal kinetic framework for Ade self-assembly. Thus, we performed a time-resolved ThT analysis, revealing a concentration-dependence. At concentrations below 32 mM Ade aggregation exhibited a sigmoidal growth with shortening lag phase as concentration increases, leading to a biphasic overshoot behaviour with progressive ThT stabilization at higher concentrations. Ade aggregation could therefore be divided into phase 1 (0 to 1 h) and phase 2 (1 h onwards) (**Fig. 1a and Fig. S3**), accounting for the initial growth and the kinetic plateauing, respectively. Remarkably, time-resolved turbidity measurements confirmed the aggregation process and exhibited similar kinetic profiles as the ones revealed by ThT, with a monotonically increase during phase 1 that plateaued afterwards (**Fig. 1b**). Sedimentation analysis demonstrated the existence of ThT-positive species that were confined to the insoluble aggregate fraction (**Fig. S2a**) and originated from the monomer depletion during phase 1 (**Fig. 1c**), indicating that net assembly ceased prior to phase 2.

The onset of phase 2 correlated with achievement of a critical phase 1 assembly load of approximately 3 g/L (~ 30 mM), calculated from monomer depletion during the first hour of reaction (**Fig. 1c**). The absence of a continuous depletion of monomeric Ade after phase 1 and the observed changes in the ThT kinetics potentially suggested that a conformational reorganisation could be triggered once the threshold concentration of phase 1 assemblies is reached. TEM revealed that fibrillar structures were already traceable at early time points. Fibrillar-like arrangements persisted throughout the whole assembly process but progressively became larger upon lateral associations and were accompanied by globular complexes at later stages (**Fig. 1d**). Consistently, FTIR indicated shifts of approximately 30 cm^{-1} in hydrogen-bonding environments between phase 1 and 2 (**Fig. 1e**), as described recently by Halasz et al, Ade polymorphs could be distinguished by FTIR due to a change in hydrogen bonding.[15] Hereby phase 1 corresponded to polymorph II and phase 2 to polymorph I. Additionally, time-resolved PXRD revealed a progressive redistribution from ~80 % polymorph II to ~80 % polymorph I (**Fig. 1f–g, Fig. S4**). Together, these data supported a model in which monomer incorporation is restricted to polymorph II formation, followed by a threshold-triggered polymorphic reorganisation of preformed assemblies towards polymorph I.

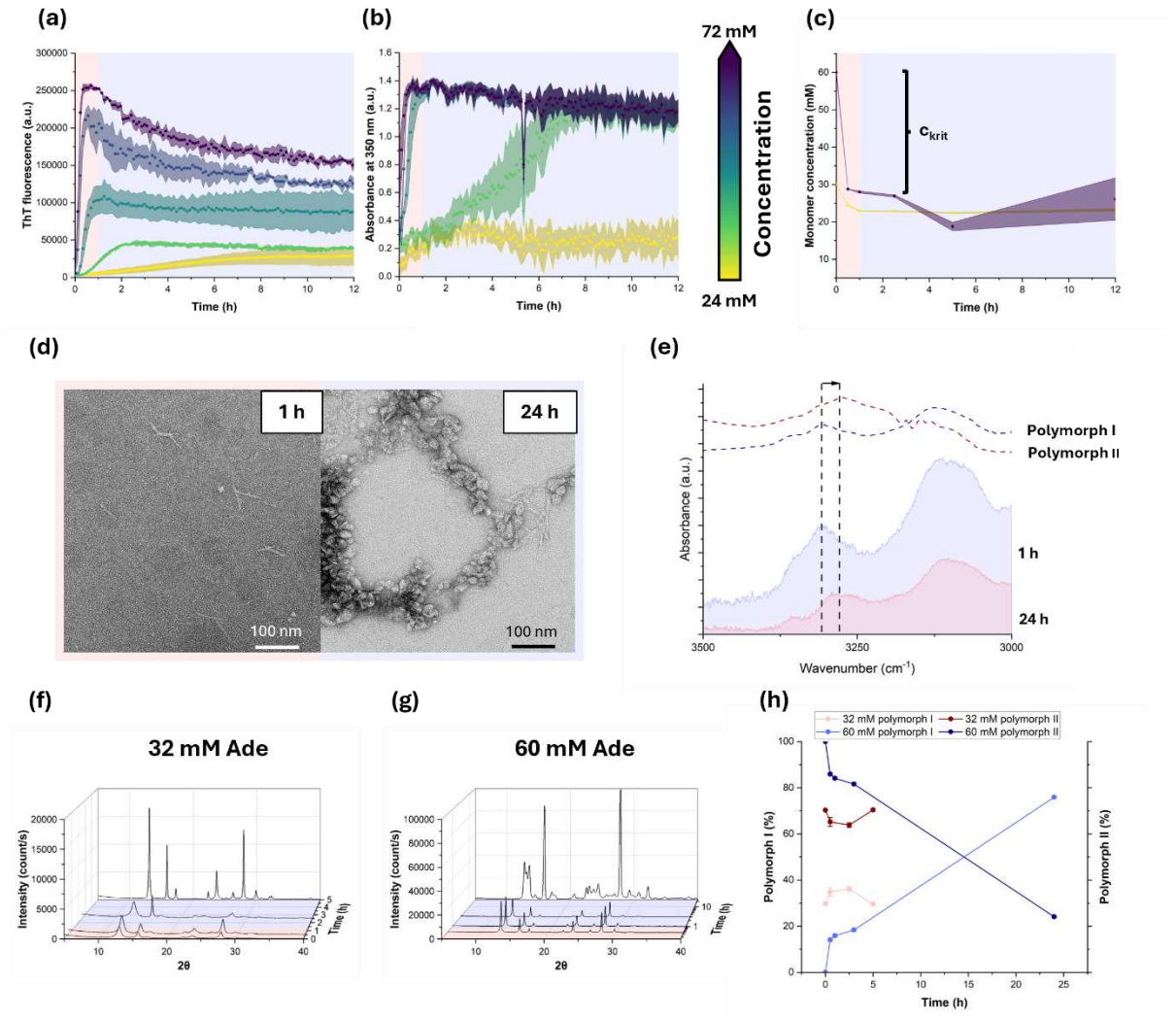

Figure 1: Self-assembly kinetics of Adenine. (a) Time dependent ThT binding kinetics, as well as **(b)** change in turbidity from 24 mM to 72 mM over time and **(c)** time dependent depletion of monomer at initial concentrations of 30 mM and 60 mM with phase 1 and 2 marked in red and blue, **(d)** TEM images of 60 mM solution at 1 h and after 24 h, **(e)** FTIR absorption as reported by the system from 3500 cm^{-1} to 3000 cm^{-1} of 60 mM Ade aggregation at 1 h and after 24 h with peakshift marked with arrows as well as literature values as dotted lines for polymorph 1 in blue and polymorph 2 in red, **(f)** PXRD pattern of 32 mM solution over time with experimental patterns, **(g)** PXRD pattern of 60 mM solution over time with experimental patterns in black and rietveld refined polymorph 1 and 2 data from CCDC database in blue and red, **(h)** Ade polymorph ratios found through Rietveld refinement of PXRD of 32 mM and 60 mM Ade samples over time

Glucosylceramide self-assembly exhibits competing aggregation pathways

To move beyond the phenomenological description of GlcCer self-assembly, we applied the same kinetic and structural analyses used to characterize Ade aggregation. In contrast to Ade dual phase self-assembly, GlcCer self-assembly exhibited three distinct kinetic phases across the full concentration range (**Fig. 2a**). An initial rapid increase in ThT fluorescence during phase 1 (0 to 0.5 h) was followed by a similarly rapid decline during phase 2 (0.5 to 1 h) and a subsequent hyperbolic increase during phase 3 (1 h onwards), indicating that GlcCer assembly does not proceed through a single monotonic pathway. As observed for Ade, sedimentation assay showed that ThT active species were confined to the insoluble fraction (**Fig. S2b**). Interestingly, turbidity kinetics showed a

similar profile to the one observed in Ade, reaching the plateau by the end of phase 2 (**Fig. 2b**) and suggesting a rapid self-assembly during phase 1 and 2. Accordingly, the correlation of a constant turbidity increase with a significant reduction in ThT signal during phase 2 could be explained by particle clustering, resulting in increased particle size but reduced ThT-accessible surface area as well as increased turbidity. The subsequent increase in ThT fluorescence during the later phase 3 suggested that the aggregated species undergone a structural reorganization, without increase in total aggregated material due to unchanged turbidity. Alternatively, the change in ThT signal could also be explained by structural rearrangements changing ThT affinity with continuous growth by further monomer incorporation. Initial velocities of phases 1 and 3 were plotted against monomer concentration (**Fig. 2c**). Both phases displayed similar concentration dependences, with comparable apparent K_m values of 59 and 73 μM^{-1}, respectively, but distinct maximal velocities. This behaviour was consistent with parallel assembly processes instead of sequential conversion of a common intermediate. TEM supported this interpretation of clustering. After phase 1, assemblies consisted predominantly of rod shaped as well as circular single sheets that increased in stacking over time, whereas fibrillar structures were observed primarily at later time points corresponding to phase 3 (**Fig. 2d**). Structural rearrangements were ruled out as the major contributor due to the fixed sheet morphology in TEM. Late formation of fibrillar GlcCer self-assembly with crystal-like features matching with phase 3 is consistent with studies by Segal et al, observing only sigmoidal growth patterns and fibrillar assemblies, without phase 1 and 2, and lack of stacked sheets.[5] Together, these findings support a model in which GlcCer initially forms kinetically favoured lipid bilayer sheets, while fibrillar assemblies arise through a slower parallel pathway that becomes dominant at later times, ultimately representing the ultimately predominant terminal morphology under our conditions. Furthermore, ThT patterns using C18 and C24 GlcCer showed only phase 1 assembly, while TEM revealed predominantly lipid bilayer sheets (**Fig. S5**).

Therefore, fibrillar assembly is heavily reliant on the correct ratio of polar headgroup and the hydrocarbon chain length.

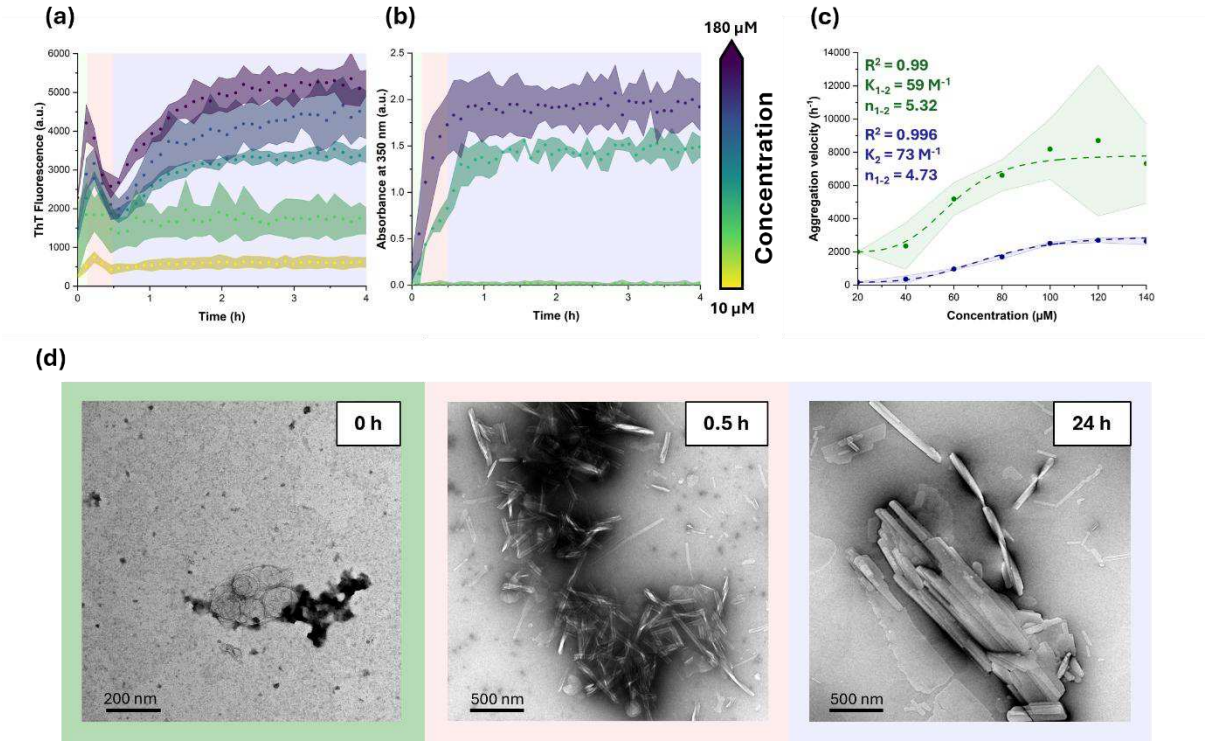

Figure 2: Self-assembly kinetics of glucosylceramide. **(a)** Time dependent ThT binding kinetics and **(b)** change in turbidity over time at concentrations from 10 µM to 180 µM GlcCer with phase 1 marked in green, phase 2 in red and phase 3 in blue, **(c)** Initial assembly velocities of phase 1 (green) and 3 (blue) plotted against initial monomer concentration fitted with Hill equations, **(d)** TEM image of 180 µM GlcCer after 0 h, 0.5 h and 24 h containing only circular sheets at 0h, both rod-like and circular sheets after 30 min, with increased clustering, and fibril and stacked lipid sheet after 24 h

Phenylalanine self-assembly is governed by concentration-dependent switching between distinct assembly states

At last, Phe self-assembly was studied similarly to Ade and GlcCer, with the additional use of time dependent CD due to the chiral nature of Phe. In contrast to the aforementioned metabolites examined, Phe displayed strong concentration-dependent self-assembly kinetics with three concentration dependent phases (**Fig. 3a–c**). At concentrations below 10 mM, ThT fluorescence sigmoidally increased to a concentration-dependent plateau, defining assembly state 1. At intermediate concentrations (15–55 mM), state 1 formation progressively weakened, as evidenced by longer lag times, reduced growth rates, and lower endpoint signals, while rapid overshoot kinetics emerged immediately after incubation was initiated. These consisted of an initial increase (state 2) followed by a fluorescence decline (state 3). Overshoot kinetics became increasingly dominant with rising monomer concentration. At high concentrations (≥55 mM), both processes persisted with little further change in state 1 assembly, and ThT-positive hydrogels formed at concentrations of 180 mM and above.

Unlike the other metabolites, Phe assemblies remained largely soluble and could not be pelleted by centrifugation. Only the hydrogel fraction, formed after prolonged incubation

at high concentrations, could be sedimented. ThT binding was detected in both pellet and supernatant fractions (**Fig. S2c**), indicating that a substantial proportion of the self-assembled species remained soluble. Still, turbidity measurements revealed striking similarity to the self-assembly behaviour seen by ThT, with similar changes in state 1 kinetics (**Fig. S6f,g**).

We later explored whether the transition from state 2 to state 3 at high Phe concentration kinetics reflected structural reorganization. Interestingly, Phe has been reported to change its dichroic spectrum when forming intermolecular contact, including π-π stacking or hydrogen bonding.[16] Therefore, we monitored the temperature-dependent changes of the molecular ordering using CD spectroscopy. Temperature-dependent measurements revealed pronounced changes in spectral intensity and peak position upon heating, consistent with substantial rearrangements in molecular packing (**Fig. S6a,b**). Due to peak shifting time-resolved CD measurements showed a concentration-dependent decrease in signal at 223 nm for samples containing ≥20 mM Phe, temporally coinciding with state 2 formation observed in ThT kinetics from 0 to 0.5 h depending on initial monomer concentration (**Fig. 3d and Fig. S6c**). The CD signal stabilized thereafter despite the continued decline in ThT fluorescence during state 3, indicating that the major molecular reorganization occurs during state 2 and that state 3 primarily reflects clustering of preformed state 2 assemblies.

TEM of endpoint samples supported the existence of structurally distinct assembly states (**Fig. 3e**). At 10 mM, where only state 1 formed, assemblies consisted of globular nanoparticles organized into extended net-like superstructures (globule chains). These globule chains remained present at 120 mM but were accompanied by distinct fibrillar structures representing state 2/3, being absent at low concentration, with fibrils forming during state 2 and further clustering in state 3, seen by the high variance in fibril thickness. The persistence of globule chains alongside the emergence of fibrils suggested that the two assembly pathways coexist rather than representing sequential conversion of a common intermediate.

Consistent with this interpretation, concentration-dependent analysis of assembly velocities revealed opposing behaviours for globule chain formation and fibrillation (**Fig. 3f**). Fibrillation followed a cooperative, Hill-type concentration dependence, whereas globule chains displayed characteristics of a negatively regulated process following a substrate inhibition dependence. These observations suggest that formation of the fibrillar state inhibits development of the globule chain architecture.

In line with these observations, PXRD did not support evidence for polymorphic interconversion, suggesting also that both species coexist. Across all concentrations and time points, diffraction patterns were best described by Phe hemihydrate 1 structure, while low-concentration samples additionally displayed diffuse low-angle scattering consistent with heterogeneous cluster formation (**Fig. S6i, and Fig. S7**). Structural evolution nevertheless mirrored the kinetic behaviour: low-concentration samples continued to increase in order over 48 h, matching the slow development of globular chains, whereas high-concentration samples underwent most structural gain within the first 5 h and showed little subsequent evolution, consistent with rapid state 2 formation (**Fig. 3g–h**). Together, these data support a model in which Phe self-assembly proceeds

through two competing pathways: *i)* a cooperative pathway yielding globule chain assemblies and *ii)* a concentration-favoured pathway generating fibrillar assemblies that subsequently cluster towards thicker fibrils until the formation of hydrogel. In contrast to Ade, these transitions occur within a common hemihydrate lattice rather than through conversion between distinct crystalline polymorphs.

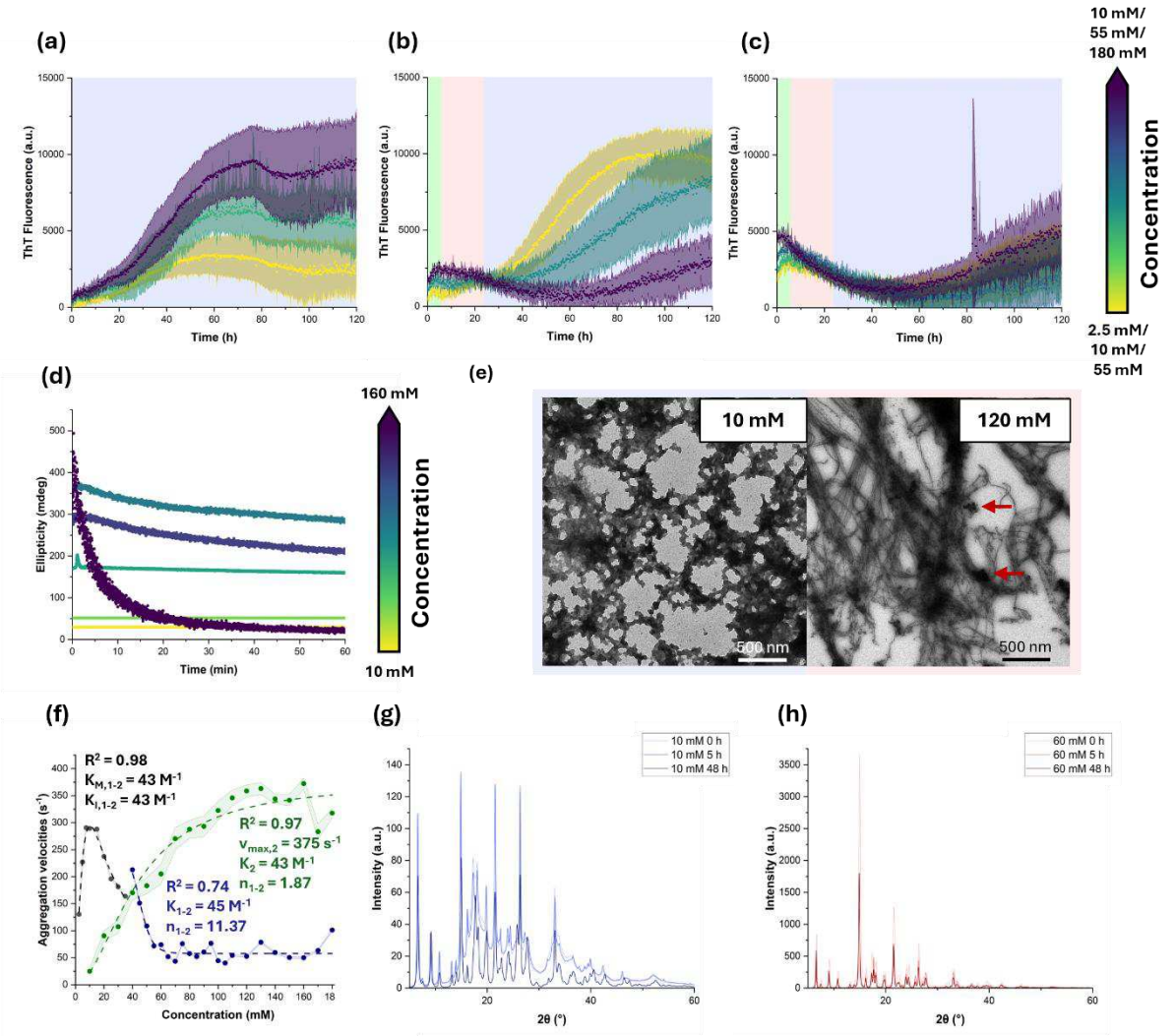

Figure 3: Self-assembly kinetics of Phenylalanine. **(a)** Time dependent ThT binding kinetics at concentrations from 2.5 mM to 10 mM, **(b)** 10 mM to 55 mM, and **(c)** 55 mM to 180 mM with state 2 and 3 formation (fibrillation) marked in red, state 1 (globule chain) formation in blue and hydrogel formation in green, **(d)** Circular dichroism of Phe at different concentrations followed over 1 h at 223.5 nm at initial concentrations of 10 mM to 160 mM, **(e)** TEM images of 10 mM and 120 mM after 180 h of incubation with red arrows indicating globule chain assemblies, **(f)** Initial assembly velocities plotted against initial monomer concentration for assembly state 1-1, 1-2 and 2 calibrated by assembly rate discovered in CD kinetic including best fits for state 1-1 (substrate inhibition), 1-2 (Hill1) and state 2 (Hill) assembly velocities, **(g)** PXRD pattern of 10 mM Phe self-assembly lyophilised after 0, 5 and 48 h and **(h)** PXRD pattern of 60 mM Phe self-assembly lyophilised after 0, 5 and 48 h

Minimal kinetic models quantitatively describe observed self-assembly behaviour

To assess whether the experimentally observed kinetic behaviours of Ade, GlcCer, and Phe could be described within a common mechanistic framework, we developed a minimal kinetic model based on primary nucleation and elongation. Secondary

processes such as fragmentation and secondary nucleation were not included, as these were not required to reproduce the experimentally observed lag phases, overshoot kinetics, or concentration-dependent saturation behaviour. The proposed model explicitly tracks both the number and mass concentration of self-assemblies.

To capture the experimentally observed sharp onset of self-assembly above defined concentration thresholds, effective critical concentration behaviour, where justified by experimental observations, was implemented phenomenologically using steep sigmoidal gating functions that approximate discontinuous transitions in a numerically stable form. This formulation was chosen to represent the experimentally observed switch-like activation of assembly regimes while preserving differentiability for numerical integration. Aggregate mass increases through nucleation and elongation, with rate constants constrained by independent experimental observables including kinetic slopes, lag-time dependence, and concentration-dependent plateau values. To enable direct comparison with experimental ThT profiles, the signal was modelled as a weighted sum of ThT-active aggregate mass, with state-dependent scaling factors accounting for differences in dye accessibility and binding affinity.

For Ade, the model was extended to include conversion from polymorph II to polymorph I corresponding to the experimentally observed polymorphic transition. Consistent with ThT measurements, polymorph I was assigned a lower apparent ThT affinity than polymorph II (**Fig. 4a**).

For GlcCer, the model incorporated an additional parallel pathway to capture the coexistence of fibrillar and sheet-like self-assemblies. This formulation was motivated by the experimentally observed similarity in concentration dependence between single sheet formation and fibrillation, inconsistent with a strictly sequential mechanism. Primary aggregation kinetics for single sheets were included to account for clustering of lipid bilayer sheets. The thermodynamic bias toward fibrillar self-assemblies was represented as a slow re-equilibration of lipid sheets back to monomer, which subsequently feeds into fibril formation (**Fig. 4b**).

For Phe, concentration-dependent negative regulation was implemented to account for the experimentally observed suppression of globule chain growth at high monomer concentrations coincident with the emergence of fibril formation. This was implemented as fibril mass dependent inhibition of the elongation rate of globular chain assemblies, reflecting competition for monomer and assembly surface rather than invoking additional reaction orders. Due to difference in ThT signal per initial monomer concentration, globular chains were assigned higher affinity than fibrillar self-

assemblies. CD-derived kinetic constraints were used to independently estimate the timescale associated with initial fibril formation (**Fig. 4c**).

Global fitting of the coupled rate equations reproduced the key features of the experimental ThT kinetics for all three metabolites, including lag phases, overshoot behaviour, and concentration-dependent plateaus. Importantly, the same minimal reaction topology was sufficient across all systems, with differences in behaviour arising from a small number of pathway-specific parameters rather than changes in model structure. While some parameters remained weakly constrained due to correlation within the differential equation system, the model consistently captured both the concentration dependence and the qualitative kinetic transitions observed experimentally (**Fig. 4d–f**).

Together, these results establish a unified, experimentally constrained kinetic framework in which chemically distinct metabolites generate divergent self-assembly behaviours through a limited and explicitly defined set of pathway-specific modifications to a common nucleation elongation scheme.

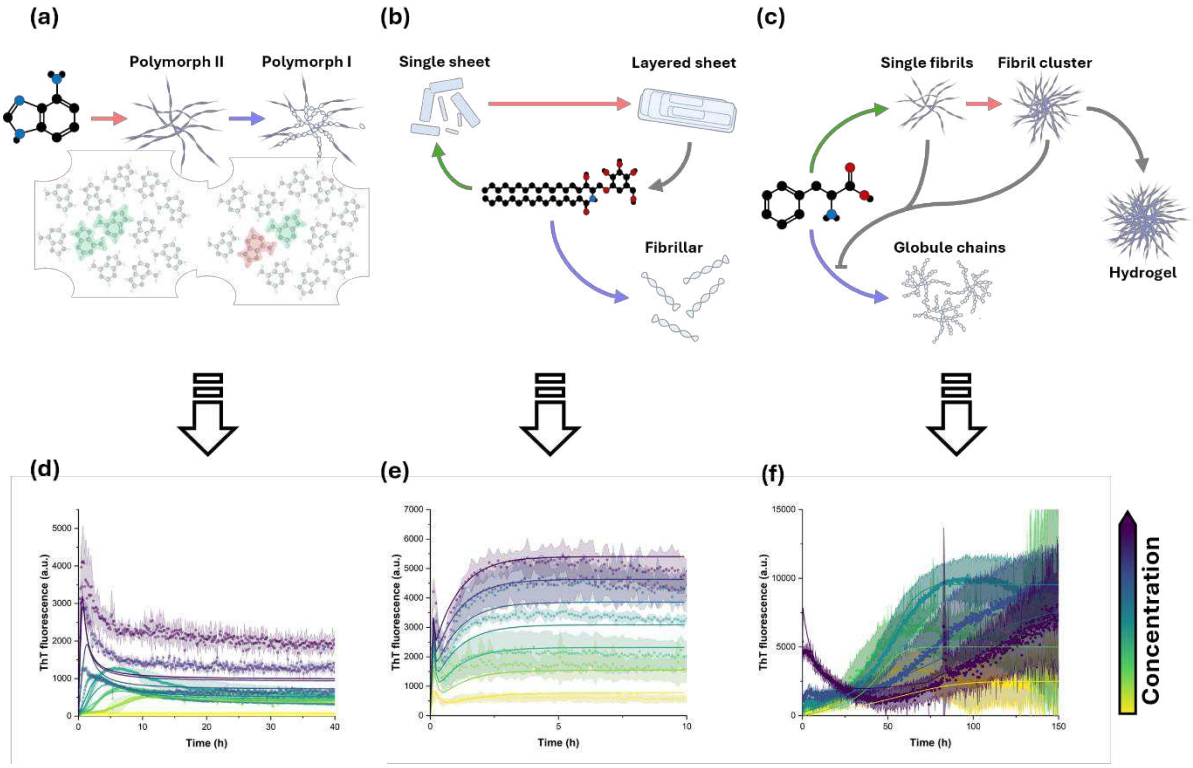

Figure 4: Kinetic modelling of metabolites' aggregation. (a-c) Model schemes for Ade, GlcCer, and Phe self-assembly, respectively, showing the proposed assembly states and transition fluxes included in the ordinary differential equation framework. **(d-f)** Global fits of the corresponding models to concentration-dependent ThT kinetics for Ade, GlcCer, and Phe

In vitro analysis of interactome revealed candidate chaperones for further investigations

Alongside our mechanistic characterization of metabolite aggregation, we screened for natural inhibitor proteins of metabolite aggregation by interactome pulldown followed by mass spectrometry. Human cells were used to identify disease-relevant modulators. In parallel, we screened bacterial cells both to test our identification pipeline against an independent proteome and to expand the candidate pool with proteins that are easy to produce for downstream applications. Cleared cell lysates were incubated in presence of different preformed metabolite self-assemblies and the interacting components inferred from proteins enriched across metabolite assembly conditions relative to non-assembled controls, enabling comparison of interaction profiles across chemically distinct aggregate states. To validate the efficiency of the protocol, we included α-synuclein fibrils, a pathological amyloid that has previously been used in the screening of molecular chaperones with anti-aggregational properties.[17]

The comparison of interaction profiles revealed an increase of cellular proteostasis components upon exposure to metabolite assemblies (**Fig. 5a, c**). In contrast to control conditions, which showed minimal non-specific association, both α-synuclein fibrils and metabolite assemblies engaged defined subsets of the chaperone systems. Importantly, interaction patterns varied across metabolite systems and assembly states within individual systems, indicating state-dependent modulation of chaperone association.

Within the bacterial interaction profile, state-associated differences were observed, including Skp, and increased association of DnaK with Phe-related profiles corresponding to state 2/3 assembly regimes. These observations indicated differential engagement of periplasmic and cytosolic chaperone modules across structurally distinct aggregate surfaces. Notably, GroEL/GroES appeared enriched compared to the negative control, especially for the mixed GlcCer assembly state sample (**Fig. 5b and Fig. S8a**).

A similar analysis of the SH-SY5Y cell interaction profile revealed broad recruitment of eukaryotic chaperone components across metabolite assemblies, indicating engagement of the human proteostasis system beyond proteinaceous amyloid-specific interactions (**Fig. 5d and Fig. S8b**). Within the α-synuclein reference profile, β-synuclein was uniquely detected, consistent with its known specificity for α-synuclein fibrillar species.

For downstream functional prioritization, we selected chaperones representing recurrent and central components across the metabolite-host interaction landscape, including DnaJC8, NPAC and Hsc70iP. Hspβ1 was additionally included due to its association with the earliest-accessible Phe assembly state, corresponding to the lowest

concentration regime of Phe assembly and capturing early-stage interaction behaviour within the system.

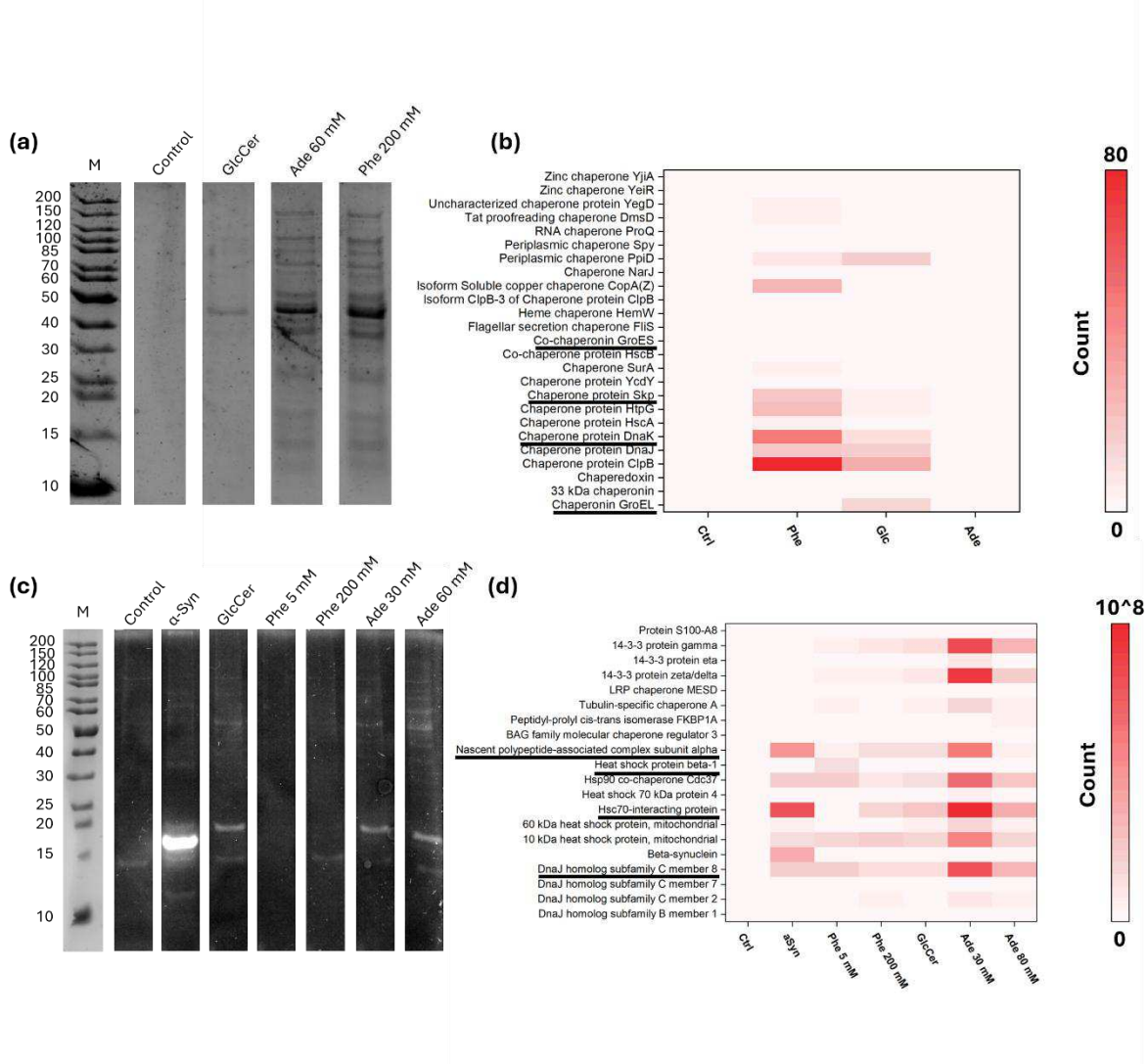

Figure 5: Metabolites' interaction profiles with cell lysates. (a) Cropped SDS-PAGE image of E. coli cell lysate incubated with buffer as negative control or preformed fibrils of 150 µM GlcCer, 60 mM Ade and 200 mM Phe, **(b)** chaperone counts compared to after interactome pulldown using bacterial lysate only as negative control with protein count from 0 to 80 and selected chaperones highlighted, **(c)** cropped and inverted SDS-PAGE image of SH-SY5Y cell lysate incubated with buffer as negative control or preformed fibrils of α-Syn, 150 µM GlcCer, 5 mM Phe, 200 mM Phe, 30 mM Ade, 60 mM Ade and **(d)** chaperone counts after interactome pulldown using SH-SY5Y lysate only as negative control and αSyn fibrils at 50 µM as positive control with protein count from 0 to 10^8 and selected chaperones highlighted

Chaperones modulate metabolite self-assembly in a state-specific manner

The effect of selected chaperones on metabolite self-assembly was then examined at different initial monomer concentrations, under conditions designed to assess the distinct assembly regimes identified for Phe, Ade, and GlcCer. Changes in ThT kinetics

were interpreted within the previously established kinetic framework to identify the assembly phase predominantly affected by each chaperone.

Recombinant production of selected human chaperones in *E. coli* yielded proteins lacking native post-translational modifications, introducing a systematic difference relative to endogenous proteostasis components. This likely contributed to quantitative differences between interaction profiles and functional inhibition assays, given the established role of such modifications in tuning chaperone interaction specificity and functional activity by phosphorylation, acetylation, methylation, ubiquitination or glycosylation, known as the "chaperone code".[18]

Chaperone effects on Ade revealed similar classes of mechanistic action, with all chaperones suppressing the overshoot behaviour at 50 mM, indicating interference with the processes underlying the polymorphic transition (**Fig. 6a and Fig. S9a–g**). However, this effect resolved into distinct kinetic modes: GroEL/ES primarily delayed entry into assembly by extending the lag phase, whereas Hsc70iP reduced the apparent growth rate, indicating modulation of distinct steps within the assembly trajectory (**Fig. S9c, d**). At 30 mM Ade, bacterial chaperones DnaK and Skp had little effect on the overall kinetic profile, whereas human chaperones like NPAC and Hsc70iP increased the final ThT signal, while Hspβ1 and GroEL/ES increased endpoint signal but delayed assembly onset. These kinetic changes were reflected in TEM analysis with all samples containing more fibrillar content than without chaperones (**Fig. 6e and Fig. S10**)

Kinetic profiles of GlcCer were affected by all chaperones of interest except Skp (**Fig. 6b and Fig. S11**). DnaK and GroEL/ES showed increased aggregation speed in the profile matching state 2 formation, while all human chaperones showed rapid onset of signal increase matching state 1 formation. All of them revealed a slow decline in ThT fluorescence until overlapping with GlcCer self-assembly without chaperone. Greater differences in interaction were seen as structural changes by TEM (**Fig. S12**). While Skp had almost no effect on kinetics, TEM revealed a change in lipid stacking architecture. Other bacterial chaperones lead to short, clustered fibrils, instead of the elongated single fibrils observed with human Hsc70iP, NPAC and Hspβ1. Additionally, NPAC lead to a distinct kind of lipid sheet not observed previously. In total, these observations clearly showed a distinct difference between bacterial and human chaperone interactions, with the first ones likely capping ends to reduce fibril lengths and thereby allowing more crosstalk compared to human chaperones binding laterally, stabilizing elongated fibrils and reducing crosstalk with each other.

To explore the full Phe self-assembly landscape four concentration regimes were selected: 10 mM (predominantly globule chain), 30–60 mM (mixed globule chain and fibrils), and 120 mM (fibril dominated). At 10 mM, human Hsc70iP selectively prolonged the lag phase without altering the subsequent growth rate (**Fig. 6c**), consistent with modulation of early nucleation rather than elongation. Bacterial chaperones including

DnaK and GroEL/ES did not suppress globular chains formation under these conditions and were instead associated with accelerated aggregation (**Fig. S13b, c**), indicating that their primary interacting mechanism does not target early nucleation events in this system.

At higher Phe concentrations, where fibril formation becomes accessible, Hsc70iP, NPAC, DnaJC8, and Hspβ1 all reduced net aggregation rates to varying extents (**Fig. 6c and Fig. S13a, d–f**). Moreover, CD spectroscopy indicated a redistribution towards fibrillation in the presence of Hsc70iP (**Fig. 6d**). Within the kinetic framework, this redistribution is expected to reduce effective accumulation of globular chain self-assemblies, thus linking chaperone binding to altered partitioning across competing self-assembly pathways rather than uniform suppression of growth. Skp and NPAC reduced aggregation speed at high Phe concentrations, consistent with interference at the level of higher-order self-assembly organisation. All chaperones inhibited hydrogel formation (**Fig. S14**) either by lateral interaction as revealed by TEM for DnaK, Hsc70iP, NPAC and Hspβ1, or reducing fibril formation as seen for GroEL/ES and Skp (**Fig. 6g and Fig. S15**).

Across all three metabolite systems, chaperone activity mapped onto a limited set of mechanistic modes, acting on either early nucleation events, growth-phase, or higher-order reorganisation processes associated with state transitions. These observations converged on a unified view in which chaperones do not act as general inhibitors of self-assembly but instead redistribute flux across a small number of competing assembly pathways. In this framework, early nucleation, growth-phase assembly, and higher-order structural reorganisation represent distinct but interconnected intervention points that are differentially targeted depending on chaperone identity and assembly regime. The

resulting behaviour is therefore best described as pathway rerouting within a shared kinetic landscape rather than uniform suppression or acceleration of aggregation.

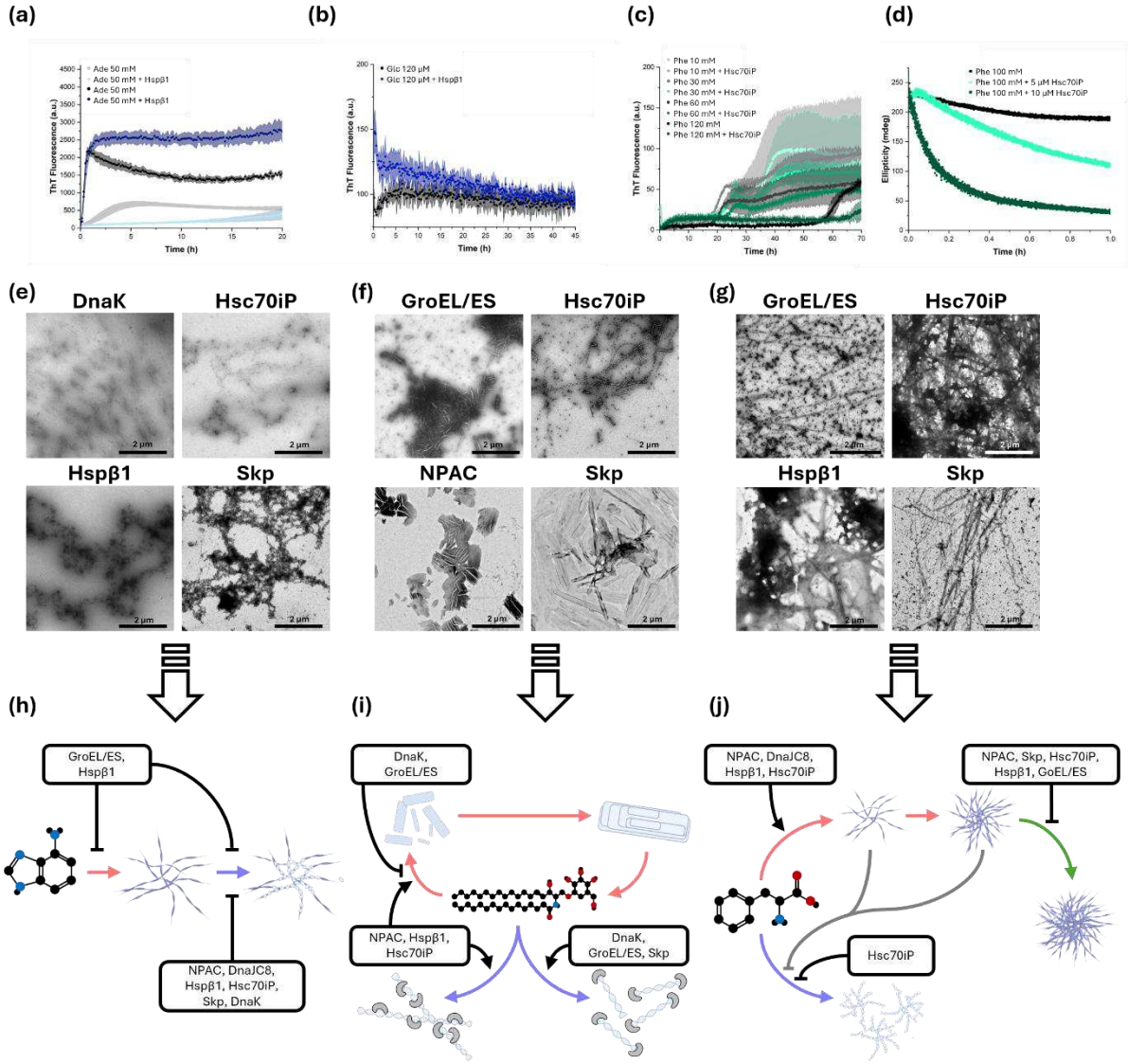

Figure 6: Effect of *Escherichia coli* and human chaperones on metabolite self-assembly. Exemplary ThT kinetics for most prominent chaperones with **(a)** 5 µM Hspβ1 on Ade at 30 and 50 mM, **(b)** 5 µM Hspβ1 on 120 µM GlcCer **(c)** 5 µM Hsc70iP on 10, 30, 60 and 120 mM of Phe, as well as **(d)** time dependent change in CD at 223 nm. Furthermore, TEM images of incubation endpoints of **(e)** Ade with DnaK, Y, NPAC, W, **(f)** GlcCer with GroEL/ES, Hsc70iP, NPAC, Skp and **(g)** Phe with GroEL/ES, Hsc70iP, Hspβ1 and Skp. Schematic representation of the chaperone effects on metabolite self-assemblies for **(h)** Ade, **(i)** GlcCer and **(j)** Phe

Discussion

This work establishes the first minimal kinetic framework to describe metabolite self-assembly across chemically diverse metabolites, using three distinct classes of metabolites: a nucleobase, an amino acid, and a lipid and provides a pipeline for identifying and testing possible interaction partners. Applying this approach to bacterial and human lysates revealed self-assembly modulation by chaperones, which subsequently steered metabolite self-assembly in kinetic assays.

Ade, a relatively rigid molecule dominated by π-stacking and hydrogen bonding, exhibited rather constrained assembly behaviour. In contrast, the more flexible GlcCer and Phe, which combine hydrogen-bonding, hydrophobic, and electrostatic interactions, accessed multiple competing assembly pathways and displayed greater kinetic and structural heterogeneity. These observations suggest that interaction diversity contributes to the observable assembly complexity. Yet protein amyloid formation generally yields comparatively simple sigmoidal kinetics. This is possibly explained by highly multivalent interaction networks being able to, under certain conditions, funnel assembly into dominant pathways, resulting in a nonlinear relationship between interaction diversity and kinetic complexity.

Across all systems, self-assembly was associated with pronounced structural plasticity and temporal evolution of aggregate states. Ade exhibited polymorphic interconversion without detectable changes in total aggregate mass, whereas GlcCer and Phe displayed coexistence of structurally and morphologically distinct assemblies that evolved over time. These observations indicate that metabolite assemblies are dynamic ensembles rather than static end products. This plasticity allows multiple assembly states to arise from single molecular species depending on concentration and time, with structural transitions feeding back into apparent kinetics through altered probe response and redistribution of assembly populations. An important consequence is that suppression or depletion of one assembly state may not prevent aggregation but instead redistribute material into alternative states with distinct structural and functional properties.

Molecular chaperones modulated the observed plasticity in a state-dependent manner *in vitro*. Interactome analyses identified enrichment of multiple bacterial and human chaperone systems across all metabolite assemblies, indicating that these non-proteinaceous aggregates are recognized by components of the cellular protein quality control network. Functional assays further showed that chaperones do not act as uniform suppressors of aggregation but instead modulate specific kinetic regimes, including nucleation, elongation, and transitions between competing assembly states. Different chaperones preferentially affected distinct metabolites and concentration regimes, consistent with sensitivity towards assembly state specific physicochemical properties, rather than molecular identity alone. In several cases, chaperones altered partitioning between competing assembly pathways rather than simply reducing aggregate formation, supporting a model in which chaperone activity acts through redistribution or redirection within a multi-pathway assembly landscape.

In the current framework of chaperone-guided quality control, proteins are recognized by exposed hydrophobic patches and structural attributes distinguishing folding intermediates from the native form. However, selectivity towards metabolite self-assemblies cannot be explained by secondary structure or other sequence-derived features. Instead, we propose an interaction mechanism guided by state-specific surface

electrostatics and form, potentially involving shielding of hydrophobic surfaces analogous to proteostasis. The molecular basis of these interactions, including whether they involve the same chaperone-binding domains as protein-client recognition, remains to be determined.

A limitation of the present study is that the metabolite concentrations required to resolve distinct self-assembly pathways exceed systemic concentrations reported in many inborn errors of metabolism. For example, phenylalanine levels in phenylketonuria typically lie in the sub-millimolar to low millimolar range[3], whereas higher concentrations were required to obtain reproducible kinetic and structural resolution. This concentration gap limits direct extrapolation to physiological conditions. Nevertheless, the *in vitro* systems allowed us to isolate intrinsic pathway behaviour, resolve competing assembly states, and define the structural transitions underlying non-canonical kinetics. By contrast, cellular environments are highly heterogeneous and characterized by macromolecular crowding, compartmentalization, phase-separated condensates, and fluctuating local metabolite concentrations, all of which can alter effective assembly equilibria. It is therefore plausible that assembly pathways requiring elevated bulk concentrations *in vitro* become accessible within confined intracellular microenvironments. Cellular components might furthermore restrict assembly plasticity as suggested by our chaperone data. Future work incorporating crowding systems, condensate models, and cellular approaches will be needed to determine how these factors reshape metabolite self-assembly *in vivo*.

The ability of molecular chaperones to alter nucleation, elongation, and pathway partitioning further provides a proof of principle that metabolite assemblies are susceptible to state-selective intervention. In this way, metabolite aggregation can be viewed within a broader framework linking metabolite accumulation, structural plasticity, and proteostasis, while highlighting control of aggregate state as a potentially underappreciated layer of metabolostasis. This raises the possibility of complementing strategies that reduce metabolite abundance with approaches that enhance

endogenous chaperone activity, mimic chaperone function, or redirect assembly towards potentially less toxic states.

Acknowledgements

D.E.O. is grateful for support from the Independent Research Foundation Denmark | Natural Sciences (grant no. 3103-00285B).

Data availability

The source data underlying Figs 1–6 and Supplementary Figs S1–S15 are provided with this paper. Raw kinetics, PXRD, CD, FTIR, and TEM data are available from the corresponding author on reasonable request.

Code availability

All custom code used in this study, comprising the Python scripts for nonlinear curve fitting and for solving and fitting the ordinary differential equation models (Methods, "Fitting"), is available at https://doi.org/10.6084/m9.figshare.34812504. The code is released under the Creative Commons Attribution 4.0 International (CC BY 4.0) license. Analyses were performed in JupyterLab using Python 3.15.2 with SciPy 1.18.1 and NumPy 2.5.4 for the fitting routines.

Competing interests

The author(s) declare no competing interests.

Author contributions

J.W. conducted the experimental work, designed the kinetic models, wrote the fitting scripts, and contributed to the overall experimental design. C.J.L. contributed to the set-up of the PXRD and FTIR measurements. C.S. performed the mass spectrometry analysis of the pulldown samples and provided the resulting hit lists. J.N. provided the human cells used in the pulldown experiments. S.P.-D. contributed day-to-day supervision, including training in instrumentation and in amyloid assembly assays. S.K., D.L.B.-Y., E.G., and D.S. contributed reagents, materials, and analytical support. M.B. supervised the PXRD and FTIR work. D.E.O. supervised the study and secured funding. J.W. and D.E.O. wrote the manuscript with input from all authors, and all authors approved the final version.

References

1 Ferreira, C. R., van Karnebeek, C. D. M., Vockley, J. & Blau, N. A proposed nosology of inborn errors of metabolism. *Genet Med* **21**, 102–106 (2019). https://doi.org/10.1038/s41436-018-0022-8

2 Stirnemann, J. *et al*. A Review of Gaucher Disease Pathophysiology, Clinical Presentation and Treatments. *Int J Mol Sci* **18** (2017). https://doi.org/10.3390/ijms18020441

3 Williams, R. A., Mamotte, C. D. & Burnett, J. R. Phenylketonuria: an inborn error of phenylalanine metabolism. *Clin Biochem Rev* **29**, 31–41 (2008).

4 Adler-Abramovich, L. *et al*. Phenylalanine assembly into toxic fibrils suggests amyloid etiology in phenylketonuria. *Nat Chem Biol* **8**, 701–706 (2012). https://doi.org/10.1038/nchembio.1002

5 Paul, A. *et al*. Glucosylceramide Associated with Gaucher Disease Forms Amyloid-like Twisted Ribbon Fibrils That Induce alpha-Synuclein Aggregation. *ACS Nano* **15**, 11854–11868 (2021). https://doi.org/10.1021/acsnano.1c02957

6 Laor, D. *et al*. Fibril formation and therapeutic targeting of amyloid-like structures in a yeast model of adenine accumulation. *Nat Commun* **10**, 62 (2019). https://doi.org/10.1038/s41467-018-07966-5

7 Sade, D., Shaham-Niv, S., Arnon, Z. A., Tavassoly, O. & Gazit, E. Seeding of proteins into amyloid structures by metabolite assemblies may clarify certain unexplained epidemiological associations. *Open Biol* **8** (2018). https://doi.org/10.1098/rsob.170229

8 Gao, X. *et al*. Human Hsp70 Disaggregase Reverses Parkinson's-Linked alpha-Synuclein Amyloid Fibrils. *Mol Cell* **59**, 781–793 (2015). https://doi.org/10.1016/j.molcel.2015.07.012

9 Ghosh, D. *et al*. The inhibitory action of the chaperone BRICHOS against the alpha-Synuclein secondary nucleation pathway. *Nat Commun* **15**, 10038 (2024). https://doi.org/10.1038/s41467-024-54212-2

10 Shaham-Niv, S. R., P.; Zaguri, D. et al. Differential inhibition of metabolite amyloid formation by generic fibrillation-modifying polyphenols. *Commun Chem* **1** (2018). https://doi.org/https://doi.org/10.1038/s42004-018-0025-z

11 Laor Bar-Yosef, D., Adsi, H. & Gazit, E. Chemical chaperones at the interface of proteostasis and metabolostasis. *Curr Opin Struct Biol* **98**, 103254 (2026). https://doi.org/10.1016/j.sbi.2026.103254

12 Saibil, H. Chaperone machines for protein folding, unfolding and disaggregation. *Nat Rev Mol Cell Biol* **14**, 630–642 (2013). https://doi.org/10.1038/nrm3658

13 Levkovich, S. A., Gazit, E. & Laor Bar-Yosef, D. The Metabolostasis Network and the Cellular Depository of Aggregation-Prone Metabolites. *Angew Chem Int Ed Engl* **62**, e202217622 (2023). https://doi.org/10.1002/anie.202217622

14 Laemmli, U. K. Cleavage of structural proteins during the assembly of the head of bacteriophage T4. *Nature* **227**, 680–685 (1970). https://doi.org/10.1038/227680a0

15 Stolar T., L. S., Požar J., Rubčić M., M. Day G., Biljan I., & Šišak Jung D., H. G., Užarević K., Meštrović E. & Halasz I. Solid-State Chemistry and Polymorphism of the Nucleobase Adenine. *Crystal Growth & Design* (2016).

16 Amdursky, N. & Stevens, M. M. Circular Dichroism of Amino Acids: Following the Structural Formation of Phenylalanine. *Chemphyschem* **16**, 2768–2774 (2015). https://doi.org/10.1002/cphc.201500260

17 Shiraz, M. G. *et al*. Young rat microbiota extracts strongly inhibit fibrillation of alpha-synuclein and protect neuroblastoma cells and zebrafish against alpha-synuclein toxicity. *Mol Cells* **48**, 100161 (2025). https://doi.org/10.1016/j.mocell.2024.100161

18 Backe, S. J., Heritz, J. A. & Mollapour, M. Hsp70 and Hsp90 post-translational modifications and translating the chaperone code. *Cell Stress Chaperones* **30**, 100118 (2025). https://doi.org/10.1016/j.cstres.2025.100118

Supplementary Files

This is a list of supplementary files associated with this preprint. Click to download.

- AllFigures.pptx
- PulldownHuman.tif